RIXS interferometry and the role of disorder in the quantum magnet $Ba_3Ti_{3-x}Ir_xO_9$

M. Magnaterra,[1] M. Moretti Sala,[2,3] G. Monaco,[4] P. Becker,[5] M. Hermanns,[6,7] P. Warzanowski,[1] T. Lorenz,[1] D. I. Khomskii,[1] P. H. M. van Loosdrecht,[1] J. van den Brink,[8,9] and M. Grüninger[1]

[1]*Institute of Physics II, University of Cologne, 50937 Cologne, Germany*
[2]*ESRF, The European Synchrotron, 71 Avenue des Martyrs, CS40220, 38043 Grenoble Cedex 9, France*
[3]*Dipartimento di Fisica, Politecnico di Milano, I-20133 Milano, Italy*
[4]*Dipartimento di Fisica e Astronomia "Galileo Galilei," Università di Padova, I-35121 Padova, Italy*
[5]*Institute of Geology and Mineralogy, Section Crystallography, University of Cologne, 50674 Cologne, Germany*
[6]*Department of Physics, Stockholm University, AlbaNova University Center, SE-106 91 Stockholm, Sweden*
[7]*Nordita, KTH Royal Institute of Technology and Stockholm University, SE-106 91 Stockholm, Sweden*
[8]*Institute for Theoretical Solid State Physics, IFW Dresden, 01069 Dresden, Germany*
[9]*Institute for Theoretical Physics and Würzburg-Dresden Cluster of Excellence ct.qmat, Technische Universität Dresden, 01069 Dresden, Germany*

(Received 25 November 2022; accepted 7 February 2023; published 10 March 2023)

Motivated by several claims of spin-orbit-driven spin-liquid physics in hexagonal $Ba_3Ti_{3-x}Ir_xO_9$ hosting Ir_2O_9 dimers, we report on resonant inelastic x-ray scattering (RIXS) at the Ir L_3 edge for different x. We demonstrate that magnetism in $Ba_3Ti_{3-x}Ir_xO_9$ is governed by an unconventional realization of strong disorder, where cation disorder affects the character of the local moments. RIXS interferometry, studying the RIXS intensity over a broad range of transferred momentum $\mathbf{q}$, is ideally suited to assign different excitations to different Ir sites. We find pronounced Ir-Ti site mixing. Both ions are distributed over two crystallographically inequivalent sites, giving rise to a coexistence of quasimolecular singlet states on Ir_2O_9 dimers and spin-orbit-entangled $j = 1/2$ moments of $5d^5$ Ir^{4+} ions. RIXS reveals different kinds of strong magnetic couplings for different bonding geometries, highlighting the role of cation disorder for the suppression of long-range magnetic order in this family of compounds.

DOI: 10.1103/PhysRevResearch.5.013167

I. INTRODUCTION

The precise theoretical definition of a quantum spin liquid has been sharpened in recent years [1], but the elusiveness of experimental realizations has remained [2–4]. Accordingly, the groundbreaking suggestion of Jackeli and Khaliullin [5] to realize Kitaev's exact spin-liquid solution in, e.g., honeycomb iridates with edge-sharing IrO_6 octahedra provoked intense activity [6–15]. Dominant bond-directional Kitaev-type exchange interactions [16] and the corresponding bond-directional character of the magnetic excitations [17] indeed were observed in Na_2IrO_3, but long-range magnetic order arises due to the existence of further exchange couplings [18–22]. In contrast, $H_3LiIr_2O_6$ was proposed to be a close realization of the Kitaev model, evading magnetic order at least down to 50 mK [23]. However, quantum chemistry calculations and density functional theory find a strong sensitivity of exchange couplings to H ion disorder and unintentional deuteration [24–26], suggesting a more conventional source of magnetic disorder.

Remarkably, several members of the hexagonal iridate family $Ba_3MIr_2O_9$ were claimed to be candidates for spin-liquid behavior [27–34]. The structure hosts triangular layers of Ir_2O_9 dimers built from face-sharing IrO_6 octahedra; see Fig. 1. The versatility of these compounds stems from the valence of the M ions, which extends from +1 to +4 [27–40]. With two holes per dimer such as in $Ba_3CeIr_2O_9$ with Ce^{4+} and Ir^{4+} ions, the ground state is nonmagnetic [35,41]. Resonant inelastic x-ray scattering (RIXS) finds quasimolecular orbitals localized on the dimers, i.e., the holes are fully delocalized over a given dimer, and the tightly bound ground-state singlet forms in a bonding orbital built from local $j = 1/2$ moments [42]. In $Ba_3InIr_2O_9$ with three holes per dimer, persistent spin dynamics were reported down to 20 mK in thermodynamic data and with local probes [30]. In RIXS, a quasimolecular $j_{\mathrm{dim}} = 3/2$ nature of the local dimer ground state was observed, establishing the compound as a cluster Mott insulator [43]. Such spin-orbit-entangled quasimolecular moments with yet to be explored exchange interactions may open up a novel route to quantum magnetism [44]. For four holes per dimer with Ir^{5+} ions, a spin-orbital liquid with weak moments has been claimed in $Ba_3ZnIr_2O_9$ [31,32]. This contradicts the nonmagnetic behavior expected for interacting Ir^{5+} $5d^4$ $j = 0$ states and again points to a quasimolecular dimer character of the electronic structure.

In $Ba_3Ti_{3-x}Ir_xO_9$, the comparable ionic radii of Ir^{4+} and Ti^{4+} yield Ti-Ir site disorder [36] (see Fig. 1) and allow for Ir

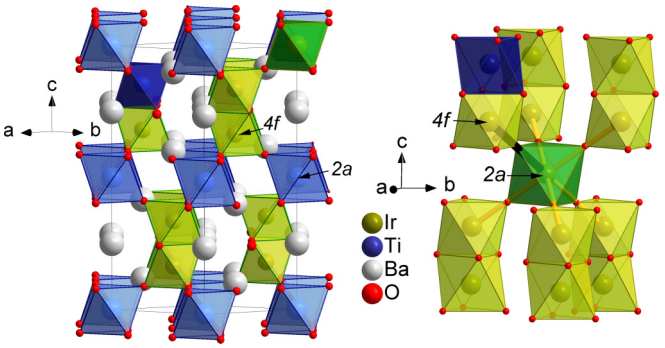

FIG. 1. Left: Hexagonal crystal structure of $Ba_3Ti_{3-x}Ir_xO_9$. In the hypothetical absence of Ir-Ti site mixing for $x = 2$, Ti (Ir) ions occupy the sites with Wyckoff position $2a$ ($4f$). Hence layers of TiO_6 octahedra (light blue) are sandwiched between layers of Ir_2O_9 dimers (light green), the latter being built from face-sharing IrO_6 octahedra. The real compound shows Ir-Ti site mixing, i.e., Ir ions also occupy $2a$ sites (dark green) and Ti ions also can be found on $4f$ sites (dark blue), the latter giving rise to $TiIrO_9$ units instead of dimers. Right: Local structure around an Ir defect ion on a $2a$ site (dark green). It is connected to six neighbors on $4f$ sites in corner-sharing geometry with 180° bonds (thick lines). In this example, five of the six neighbors belong to Ir_2O_9 dimers, but there is a single Ir^{2a}-Ir^{4f} pair (thick black line) where the Ir ion on the $4f$ site is part of an $IrTiO_9$ unit.

contents different from $x = 2$. This compound has been discussed as a spin-liquid candidate for $x \in \{0.5, 1, 2\}$ [27–29], and the average magnetic moment was reported to *decrease* upon increasing the concentration of magnetic Ir^{4+} ions [28]. For $x = 1$, a triangular lattice of Ir^{4+} $j = 1/2$ moments would be formed in the hypothetical case of perfect cation order with all Ti ions occupying dimer sites. This is attractive from the point of view of theory since novel quantum phases are predicted for a triangular Heisenberg-Kitaev model [45,46]. To understand the magnetism of $Ba_3Ti_{3-x}Ir_xO_9$, one needs to address both disorder and the role of quasimolecular dimer states. We show below that RIXS is the ideal tool to achieve this goal.

In L-edge RIXS measurements on $Ba_3Ti_{3-x}Ir_xO_9$ with $x \in \{0.3, 0.5, 1.5, 1.8\}$, we find a coexistence of quasimolecular Ir_2 dimer states and single-site $j = 1/2$ moments, providing a clear fingerprint of substantial Ir-Ti site mixing. The quasimolecular dimer character is nailed down via a double-slit-type sinusoidal interference pattern in the RIXS intensity as a function of the transferred momentum $\mathbf{q}$, in agreement with previous results on $Ba_3CeIr_2O_9$ and $Ba_3InIr_2O_9$ [42,43]. Additionally, the study of such interference patterns allows us to identify a RIXS peak at 0.15 eV with site-mixing-induced magnetic excitations of Ir moments on M sites ($2a$) that are strongly exchange coupled to neighboring dimer sites ($4f$) via 180° bonds; see Fig. 1. The $2a$-$4f$ bonding geometry is very similar to the case of Sr_2IrO_4 [47,48], which roughly explains the energy scale of 0.15 eV. The ability to disentangle the contributions of different Ir sites in such a strongly disordered system demonstrates the power and versatility of RIXS interferometry.

Our findings on $Ba_3Ti_{3-x}Ir_xO_9$ highlight the unconventional role that disorder may play in a cluster Mott insulator. Removing a magnetic ion from a cluster such as a dimer does not create a usual vacancy but strongly changes the moment's character as well as the relevant (exchange) interactions. In our example of dimers, the character changes from quasimolecular $j_{\mathrm{dim}} = 0$ to single-site $j = 1/2$ moments. For perfect cation order, magnetic interactions for the Ir_2 dimers range from very weak for interdimer exchange couplings up to about 1 eV for intradimer singlet-to-triplet excitations, but cation disorder yields pairs of local moments with exchange coupling of about 0.15 eV. The physics of $Ba_3Ti_{3-x}Ir_xO_9$ thus is governed by a complex mixture of Ti-Ir site disorder, the statistical coexistence of different magnetic moments, and very different magnetic couplings.

II. EXPERIMENT

Crystals of $Ba_3Ti_{3-x}Ir_xO_9$ were grown using $BaCO_3$, IrO_2, and TiO_2 as educts and $BaCl_2$ as melt solvent. After the growth process the crystals were mechanically separated from the flux and washed with cold H_2O. We studied samples with an Ir content $x \in \{0.3, 0.5, 1.5, 1.8\}$ as determined by energy dispersive x-ray spectroscopy (EDX). The crystals with $x = 0.3$ and 0.5 resulted from one growth experiment with a ratio $IrO_2 : TiO_2 = 1 : 2$, while the crystals with $x = 1.5$ and 1.8 were obtained for $IrO_2 : TiO_2 = 2 : 1$ and otherwise identical growth parameters. This indicates an effective distribution coefficient $k_{\mathrm{eff}} = c_{\mathrm{Ir}}^{\mathrm{cryst}}/c_{\mathrm{Ir}}^{\mathrm{melt}} < 1$ for the concentration of Ir ions in the crystal and the melt, respectively. This causes Ir depletion in the crystals with respect to the melt and thus Ir accumulation in the melt as a function of time. Crystals nucleating later in the course of the unseeded growth experiment grow in a melt that is enriched with Ir, giving rise to a larger Ir content x. From single-crystal x-ray diffraction and structure refinements, room-temperature lattice constants of $a = (5.7103 \pm 0.0011)$ Å and $c = (14.1516 \pm 0.0029)$ Å were obtained in the hexagonal space group $P6_3/mmc$ for two samples from the two different batches. The magnetic susceptibility was measured in a commercial superconducting quantum interference device (SQUID) magnetometer (Quantum Design MPMS).

RIXS measurements were performed in horizontal scattering geometry at the Ir L_3 edge at beamline ID20 at the European Synchrotron Radiation Facility (ESRF) [49,50]. We measured on the (001) surface for $x = 0.3$ and $x = 1.8$ and on the (100) surface for $x = 0.5$ and $x = 1.5$. Our study highlights the information contained in the $\mathbf{q}$ dependence of the RIXS intensity. For the sinusoidal intensity modulation of Ir_2O_9 dimer excitations, the sample orientation is mainly relevant for the accessible range of q_c, the component of $\mathbf{q}$ parallel to the c axis. Particularly large values of q_c can be reached on the (001) surface, while the (100) surface allows us to cover the range around $q_c = 0$; see Sec. V B. To determine the resonance behavior, we collected a low-resolution (0.4 eV) RIXS map at 300 K on $Ba_3Ti_{1.2}Ir_{1.8}O_9$; see Sec. V. Focusing on intra-t_{2g} excitations, we choose an incident energy of 11.215 keV. At $T = 20$ K, we measured RIXS spectra with an energy resolution of 27 meV by scanning the energy loss at constant $\mathbf{q}$. The RIXS spectra were normalized with respect to the incident flux and the acquisition time. Furthermore, we collected $\mathbf{q}$ scans at constant energy loss. The intensity was

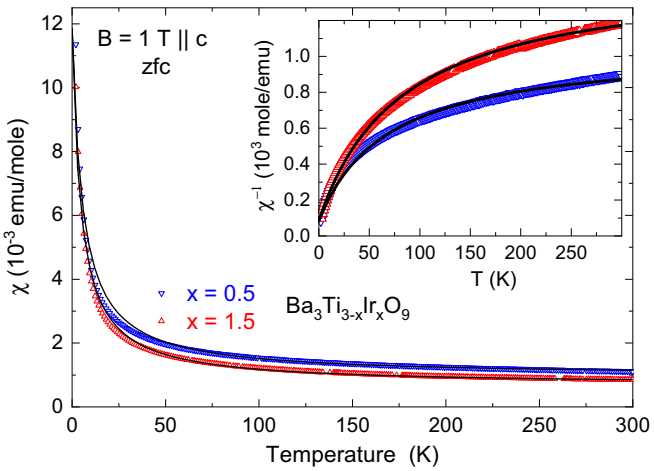

FIG. 2. Magnetic susceptibility $\chi(T)$ of $Ba_3Ti_{3-x}Ir_xO_9$ for $x = 0.5$ and 1.5, measured on the same samples as studied in RIXS. The inset displays $1/\chi$ vs T. Solid lines are Curie-Weiss fits according to Eq. (1) with fixed $\mu_{\rm eff} = 1.73\ \mu_{\rm B}$.

corrected for self-absorption effects, compensating the different paths traveled by the photons within the absorbing sample for different scattering geometries [51]; see Appendix A.

The two sites of a dimer are connected by the vector $\mathbf{d} = (0, 0, d)$. As discussed below, the quasimolecular dimer features are characterized by a RIXS intensity that is modulated with a period $2Q_d = 2\pi/d$ which is incommensurate with the Brillouin zone. Accordingly, we denote reciprocal space vectors in absolute units while the indices $(h\ k\ l)$ are given in reciprocal lattice units (r.l.u.).

III. CATION DISORDER

In the absence of cation disorder, the M ions in $Ba_3MIr_2O_9$ occupy the single-layer $2a$ sites while the Ir ions are located on the dimer $4f$ sites; see Fig. 1. In $Ba_3MIr_2O_9$, perfect cation ordering is achieved for a significant difference in ionic radii of M^{4+} and Ir^{4+} [36,42]. In contrast, site mixing of Ti^{4+} and Ir^{4+} has been observed in $Ba_3Ti_{3-x}Ir_xO_9$ [36], which can be rationalized by the fact that Ti^{4+} and Ir^{4+} show not only the same valence but also similar ionic radii. On the $2a$ position, the Ir-Ti site mixing in $Ba_3Ti_{3-x}Ir_xO_9$ was reported to amount to about 6 and 21% for $x = 1$ and 2, respectively [27–29,36], suggesting that Ir preferably occupies $4f$ dimer sites. Within the dimers, there is no preferential occupation of Ir^{4+} and Ti^{4+} between the two crystallographically equivalent dimer sites [27–29,36].

IV. MAGNETIC SUSCEPTIBILITY

The magnetic susceptibility $\chi(T)$ is plotted in Fig. 2 for two samples with $x = 0.5$ and 1.5. After zero-field cooling (zfc), the data were obtained in a field of 1 T upon heating, but there is no difference between these data and the corresponding data obtained after field cooling in 1 T (not shown). Our data do not provide any indication for long-range magnetic order, and the overall magnetic signal does not increase from $x = 0.5$ to $x = 1.5$, i.e., upon enhancing the content x of magnetic Ir^{4+} ions by a factor of 3. The latter at first sight is surprising, but it agrees with previous results [28]. This unusual behavior can be explained using our RIXS results (see Sec. V), which demonstrate strong site disorder of Ir^{4+} and Ti^{4+} ions with respect to the occupation of the $(2a)$ M sites and the $(4f)$ dimer sites (see Fig. 1), in combination with the formation of nonmagnetic singlets in the case of two Ir^{4+} ions occupying both $4f$ sites within a dimer. Therefore the overall magnetic susceptibility consists of the superposition of different Curie-Weiss and Van Vleck contributions based on local moments on $2a$ or $4f$ sites and dimers. Because a reliable quantitative separation of the various contributions to $\chi(T)$ is not possible, we restrict ourselves to a strongly simplified effective Curie-Weiss model, which neglects a possible temperature dependence of the effective magnetic moments by setting $\mu_{\rm eff} = 1.73\ \mu_{\rm B}$ of a spin 1/2. Moreover, we assume temperature-independent Van Vleck terms which are included in a constant background susceptibility χ_0,

$$\chi(T) = n\frac{N_{\rm A}\ \mu_{\rm eff}^2}{3k_{\rm B}(T-\theta_W)} + \chi_0. \tag{1}$$

This yields three adjustable parameters, where n denotes the amount of localized magnetic moments, θ_W measures their effective interaction strength, and χ_0 is the sum of the overall Van Vleck contribution and the core diamagnetism. As shown in Fig. 2, the measured data can be reasonably well described by the simplified model of Eq. (1) with the parameter set $n = 0.16$, $\theta_W = -5.5$ K, and $\chi_0 = 9.5 \times 10^{-4}$ emu/mole for $x = 0.5$, while we obtain $n = 0.14$, $\theta_W = -4.7$ K, and $\chi_0 = 6.8 \times 10^{-4}$ emu/mole for the sample with $x = 1.5$. The two parameter sets, with weakly antiferromagnetic Weiss temperatures and comparable χ_0 values, are very similar, as expected due to the very similar $\chi(T)$ data. In view of the very different values of x, the very similar results for n are remarkable, but our RIXS data confirm a similar density of local moments in the two samples; see Sec. V A. This indicates that for large x the vast majority of Ir^{4+} ions form singlet dimers.

V. RIXS RESULTS

Resonance behavior. In RIXS, the cross section of spin and orbital excitations is boosted by tuning the incident energy $E_{\rm in}$ to a specific absorption edge, in our case the Ir L_3 edge. To optimize $E_{\rm in}$, we start by examining a resonance map of $Ba_3Ti_{1.2}Ir_{1.8}O_9$, i.e., we measure low-resolution (0.4 eV) RIXS spectra for $E_{\rm in}$ in the range from 11.213 to 11.222 keV; see Fig. 3. For all of the observed inelastic features, the energy loss is independent of $E_{\rm in}$ while the RIXS intensity exhibits pronounced resonance behavior. For energy loss larger than 5 eV, we observe charge-transfer excitations. The strongest RIXS peak is located at about 3 eV energy loss and corresponds to excitations from a t_{2g} orbital to an e_g^σ level. It hence is a measure of the crystal-field splitting $10\,Dq$. This peak shows maximum resonance enhancement for an incident energy $E_{\rm in} \approx 11.218$ keV. In the following, we focus on the intra-t_{2g} excitations below about 1.2 eV and accordingly choose $E_{\rm in} = 11.215$ keV.

Features in the RIXS spectra. We study RIXS data of $Ba_3Ti_{3-x}Ir_xO_9$ for $x \in \{0.3, 0.5, 1.5, 1.8\}$. A first overview of the detected features is given by the RIXS spectra shown in Figs. 4 and 5 for selected values of $\mathbf{q}$. In Fig. 4 we address the

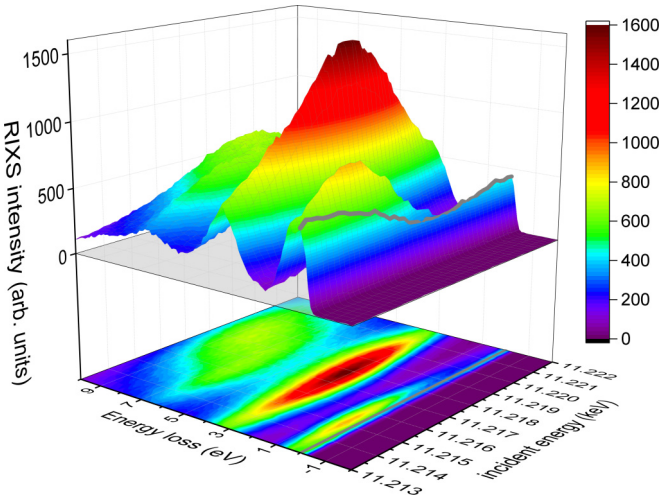

FIG. 3. RIXS resonance map of $Ba_3Ti_{1.2}Ir_{1.8}O_9$ measured at 300 K for transferred momentum $\mathbf{q} = (0\ \ 0\ \ 18.5)$ r.l.u. The upper part depicts a three-dimensional (3D) plot of the RIXS intensity as a function of both incident energy E_{in} and energy loss. The lower part shows the same data as a color plot, where the energies are easier to identify. The dominant RIXS peak at 3 eV energy loss corresponds to excitations to e_g^σ orbitals which are resonantly enhanced for an incident energy of about 11.218 keV. The intra-t_{2g} excitations below about 1.2 eV are maximized for an incident energy of 11.215 keV. The thick gray line is the elastic line at zero loss.

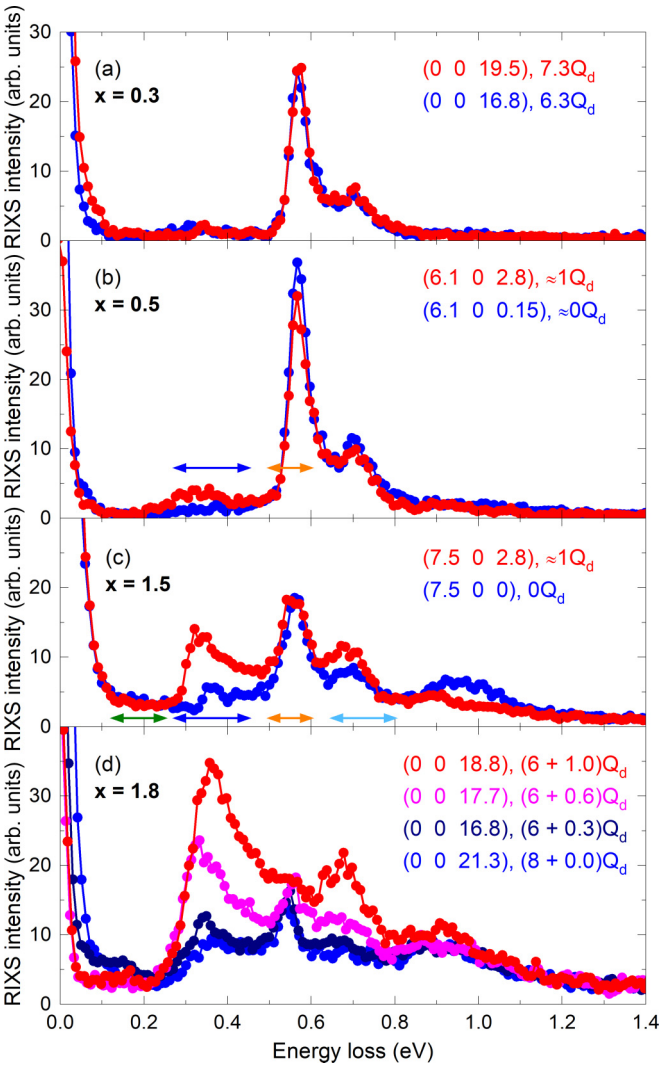

FIG. 4. (a)–(d) RIXS spectra of $Ba_3Ti_{3-x}Ir_xO_9$ at $T = 20$ K, showing the coexistence of single-site and dimer excitations at least for $x \geqslant 0.5$. For each x, we compare data for different l. For $x = 0.3$ and 1.8 we measured on the (001) surface with $h = k = 0$ and large l, while the data for $x = 0.5$ and 1.5 were collected on the (100) surface with large h and smaller l. For small x, the two-peak structure of the spin-orbit exciton dominates, a mark of single-site $j = 1/2$ moments. For large x, the broad features above 0.2 eV correspond to quasimolecular excitations on Ir_2 dimers, which is reflected in the sinusoidal q_c dependence of the intensity with a period $2Q_d = 2\pi/d$; cf. Fig. 6. Compared with an intensity minimum at $m \cdot 2Q_d$ with integer m, the data in (d) correspond to $0Q_d$, $0.3Q_d$, $0.6Q_d$, and $1.0Q_d$. The arrows in (b) and (c) denote the integration ranges used in Fig. 6.

behavior as a function of q_c, the component of $\mathbf{q}$ parallel to the c axis. To identify dimer features (see below), we express q_c in terms of $Q_d = \pi/d \approx 5.3 \times \pi/c$. In contrast, Fig. 5 highlights the h dependence for $q_c \approx 6.3Q_d$ and $7.3Q_d$ for $x = 1.8$.

We will show below that the RIXS spectra reveal the coexistence of three different kinds of excitations. In Sec. V A, we address the contribution of individual $j = 1/2$ sites, which dominates for small x; see Fig. 4(a). In Sec. V B, we discuss the excitations on structural dimers with quasimolecular states. These dimer excitations set in above about 0.2 eV and prevail for large x. Accordingly, the overall line shape changes strongly as a function of x; see Fig. 4. Finally, Sec. V C addresses a further, weak RIXS peak at about 0.15 eV that we find for $x = 1.5$ and 1.8. This peak is most evident in Fig. 5 as the only feature with a particular h dependence of the intensity. In the data of Fig. 4(d), the presence of this weak low-energy RIXS peak can be highlighted by a closer examination of the tail of the elastic line; see Appendix B. Using RIXS interferometry, we will demonstrate that this 0.15 eV feature corresponds to magnetic excitations related to Ir ions on 2*a* sites.

A. Individual $j = 1/2$ moments

For small x, the RIXS spectra provide an unmistakable fingerprint of diluted $5d^5$ Ir^{4+} sites; see Fig. 4(a) and 4(b). The data predominantly show the well-known two-peak structure of the so-called spin-orbit exciton, i.e., excitations from local $j = 1/2$ moments to the $j = 3/2$ excited quartet state which is, however, split by the trigonal crystal field [52]. Features similar to the two narrow peaks at 0.57 and 0.70 eV were observed in many iridates with (weakly) interacting $j = 1/2$ moments [53–60]. Compared with, e.g., honeycomb Na_2IrO_3 or square-lattice Sr_2IrO_4 [47,48,53], the small linewidth of the pronounced peak at 0.57 eV underlines that interactions between individual $j = 1/2$ moments are weak in $Ba_3Ti_{3-x}Ir_xO_9$.

Typical for iridates, $Ba_3Ti_{3-x}Ir_xO_9$ shows a strong cubic crystal-field splitting $10\,Dq \approx 3$ eV between t_{2g} and e_g^σ states; see Fig. 3. In this case, the physics of intra-t_{2g} excitations on

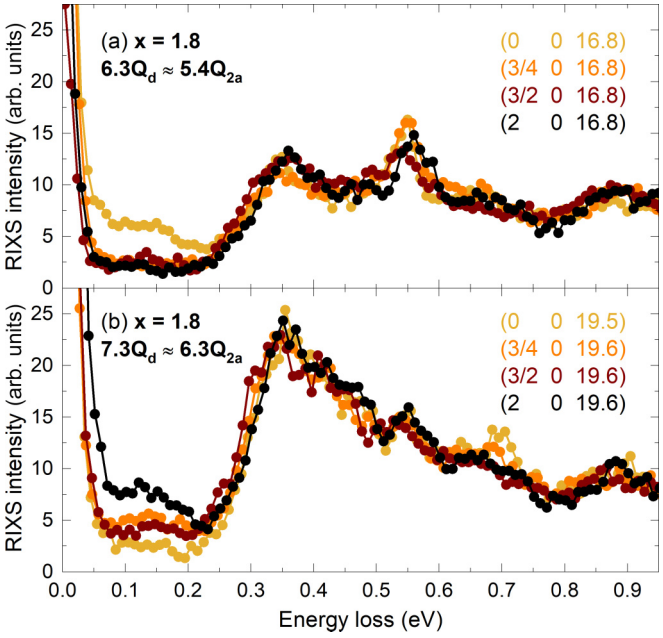

FIG. 5. RIXS spectra of $Ba_3Ti_{1.2}Ir_{1.8}O_9$ for $0 \leqslant h \leqslant 2$ at $T = 20$ K. For the dimer excitations above 0.2 eV, the different intensities in (a) and (b) reflect the $\sin^2(q_c d/2)$ modulation. With $Q_d = \pi/d$, the value $l = 16.8$ (19.6) corresponds to $q_c \approx 6.3Q_d$ ($7.3Q_d$), which is close to a minimum (maximum); see Figs. 4 and 8. Only the weak 0.15 eV peak exhibits a pronounced h dependence. It corresponds to a magnetic excitation that involves an Ir ion on a $2a$ site, giving rise to an intensity modulation along h, k, and l; see Sec. V C. For constant h and k, it shows a period of $2Q_{2a} \approx 2.3Q_d$. In contrast to the dimer features above 0.2 eV, its intensity for $h = k = 0$ is enhanced for $l = 16.8$ but suppressed for $l = 19.6$.

a single t_{2g}^5 site is well described by the Hamiltonian [52]

$$H_{\text{single}} = \lambda\, \mathbf{S} \cdot \mathbf{L} + \Delta_{\text{CF}} L_z^2, \tag{2}$$

where λ and Δ_{CF} denote spin-orbit coupling and the trigonal crystal field, respectively. In terms of an IrO_6 point-charge model, trigonal elongation or contraction of the oxygen octahedron corresponds to positive or negative Δ_{CF}, but in $Ba_3Ti_{3-x}Ir_xO_9$ with face-sharing octahedra the sign also depends on covalency and interactions with further ions [61]. Based on the crystal structure, $\Delta_{\text{CF}} \neq 0$ is already expected for undistorted octahedra. Depending on the sign of Δ_{CF}, the observed peak energies of 0.57 and 0.70 eV yield either $\lambda = 0.41$ eV and $\Delta_{\text{CF}} = -0.18$ eV or $\lambda = 0.40$ eV and $\Delta_{\text{CF}} = 0.23$ eV. Since the Hamiltonian in Eq. (2) only deals with t_{2g} electrons, it yields an effective value of λ that slightly depends on $10\,Dq$. Our solutions $\lambda = 0.40$ or 0.41 eV fall well within the range reported in RIXS on Ir oxides [42,43,47,48,53–57,62–67].

With Ir^{4+} ions occupying $4f$ and $2a$ sites, one may expect different values of Δ_{CF}, and these may cause a further splitting of the peaks at 0.57 and 0.70 eV. As stated above, only about 6% of the $2a$ sites were reported to be occupied by Ir ions for $x = 1$, but this value increases to 21% for $x = 2$ [27–29,36]. For large x, a detailed analysis of the spin-orbit exciton peaks is hindered by the additional presence of dimer features in the spectra. However, the enhanced width of the 0.57 eV peak for $x = 1.5$ possibly reflects different values of Δ_{CF} on the two sites.

Comparing $x = 0.3$ and $x = 0.5$, the RIXS intensity of the peak at 0.57 eV increases with x (see Fig. 4), and the relative intensity roughly agrees with the relative Ir concentration. In the same spirit, the integrated intensity of the 0.57 eV peak for $x = 1.5$ amounts to about 80% of the value for $x = 0.5$, which roughly agrees with the ratio of the n values determined from $\chi(T)$; cf. Sec. IV. However, the RIXS matrix elements depend on the measurement geometry and the sample orientation, and the intensity is further affected by the surface quality. Therefore we refrain from a more detailed quantitative comparison of the RIXS intensities obtained on different samples. In contrast, our analysis focuses on the presence or absence of a $\mathbf{q}$-dependent intensity modulation and its period, as discussed in the next section. We nevertheless emphasize that the strong peak at 0.57 eV is observed for all x, demonstrating the presence of individual $j = 1/2$ sites even for large x when the response is dominated by dimers.

B. Quasimolecular dimer excitations

For $x = 0.5$, at most 1/4 of the $4f$ dimer sites can be occupied by Ir ions, and this number is even smaller if Ir ions also occupy the $2a$ sites. The pronounced change in the line shape of the RIXS spectra with increasing x (cf. Fig. 4) reflects an increasing density of Ir_2 dimers along with a dramatic difference of the electronic structure of dimers compared with weakly interacting $j = 1/2$ moments. For $x = 1.8$, the strongest RIXS peak is observed at about 0.35 eV, and the spectra for $x = 1.5$ and 0.5 reveal corresponding features at the same energy, i.e., dimers are already formed for $x = 0.5$.

In spectroscopy on crystalline materials, studies of the $\mathbf{q}$-dependent properties often focus on the dispersion $\omega(\mathbf{q})$ of the excitation energy. For excitations localized on a dimer, however, the key feature is the $\mathbf{q}$ dependence of the RIXS *intensity*, allowing us to unravel the quasimolecular character of a given excitation [42,43]. For an individual $j = 1/2$ moment on a single site, neglecting interactions, the local excitation to $j = 3/2$ states does not show any $\mathbf{q}$ dependence. The spin-orbit exciton peaks at 0.57 and 0.70 eV support this picture for $x = 0.3$ and 0.5 for two different $\mathbf{q}$ points; see Fig. 4. Addressing the $\mathbf{q}$ dependence more explicitly, Fig. 6 shows that the integrated RIXS intensity of the strong 0.57 eV peak is roughly independent of q_c over many Brillouin zones. This is observed for both $x = 0.5$ and 1.5. In contrast, the sinusoidal modulation of the RIXS intensity integrated around 0.35 eV (dark blue symbols in Fig. 6) provides an unambiguous proof of the quasimolecular character of the orbitals involved in this excitation [42], again both for $x = 0.5$ and for $x = 1.5$. The data are well described by

$$I_f(q_c) = \left(a_0 + a_1 q_c + a_2 q_c^2\right) \sin^2(q_c\, d/2) + c_0 + c_1 q_c, \tag{3}$$

where q_c is the $\mathbf{q}$ component parallel to the c axis, $\mathbf{d} = (0, 0, d)$ connects two Ir $4f$ sites within a dimer, and the a_i and c_i are fit parameters describing the modulation amplitude and an offset, respectively. Central to our study is the $\sin^2(q_c\, d/2)$ modulation pattern that reflects the two-site interference character sketched in the inset of Fig. 6(a) and discussed below. The period $2Q_d = 2\pi/d$ provides a measure of the intradimer

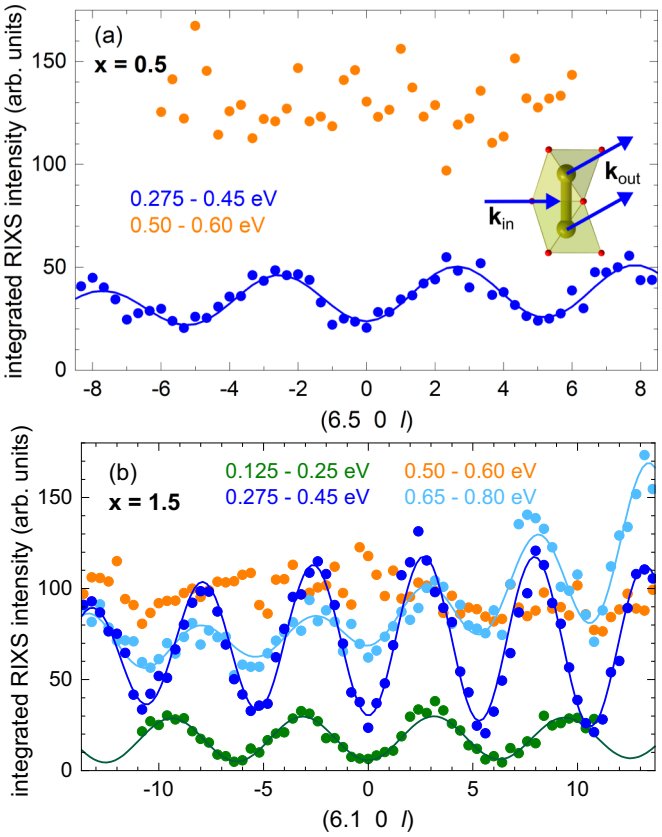

FIG. 6. RIXS interference patterns as a function of l for $x = 0.5$ (a) and 1.5 (b). Measuring on a (100) surface with c in the scattering plane allows us to cover a large range of l that includes $l = 0$. Data were corrected for self-absorption [51] (see Appendix A) and integrated over the indicated energy ranges. The local, single-site character of the spin-orbit exciton yields roughly constant intensity around 0.57 eV (orange). In contrast, the $\sin^2(q_c\, d/2)$ modulation of the 0.35 eV peak (dark blue) with period $2Q_d = 2\pi/d$ demonstrates two-site interference as sketched in the inset of (a) and hence a quasimolecular dimer character. The larger period observed for integration below 0.25 eV for $x = 1.5$ [green in (b)] unveils a different microscopic origin related to Ir ions on $2a$ sites; see Sec. V C. For each point, the integration time was 20 s (orange) and 60 s (blue) in (a) and 30 s in (b).

Ir-Ir distance d. We find $2Q_d = (5.34 \pm 0.04) \times 2\pi/c$, which is equivalent to $d = (2.66 \pm 0.02)$ Å at 20 K, in agreement with the value 2.65 Å determined in elastic x-ray diffraction at 300 K [36]. The observed period hence firmly establishes that the corresponding RIXS features arise from quasimolecular states of the Ir_2O_9 dimers. We do not analyze the detailed $\mathbf{q}$ dependences of amplitude and offset in Eq. (3), which mainly reflect the change in the experimental scattering geometry that is necessary to vary $\mathbf{q}$ over a large range, giving rise to a change in polarization factors. At the same time, the scattering geometry determines self-absorption effects [51], which, however, have been corrected in our data; see Appendix A.

For $x = 1.5$ and integration from 0.65 to 0.80 eV, we find a modulation with the same period as around 0.35 eV but reduced amplitude (light blue symbols in Fig. 6), suggesting that dimer excitations overlap with the single-site 0.70 eV peak. Remarkably, integration below 0.25 eV (green symbols in Fig. 6) reveals a period that is about 17% larger, pointing towards a different origin of the corresponding excitation. It stems from Ir pairs where one Ir ion is located on a $2a$ site; see Sec. V C.

The sinusoidal intensity modulation described by Eq. (3) was also observed in RIXS on magnetic excitations in honeycomb Na_2IrO_3, where dominant Kitaev interactions yield dynamical spin-spin correlations that are restricted to nearest neighbors on a bond, forming the dynamical magnetic equivalent of a dimer [17,68]. A sinusoidal modulation in $\mathbf{q}$ space reflects the Fourier transform of a dimer. In the case of RIXS, this intensity modulation reveals the dynamical structure factor of a dimer excitation. In other words, it is equivalent to an inelastic realization of a double-slit-type interference pattern [42,69–72]. To calculate the corresponding total RIXS amplitude $A_f(\mathbf{q})$, one has to sum up all scattering processes that lead to a given final excited state $|f\rangle$. The RIXS process at the Ir L_3 edge proceeds via an intermediate state with a $2p$ core hole that is strongly localized on a given Ir site. In the case of Ir_2O_9 dimers with quasimolecular orbitals, the scattering process may occur on each of the two Ir sites $\mathbf{R}_i$ over which the holes are delocalized in both the ground state $|0\rangle$ and the excited state $|f\rangle$. As sketched in the inset of Fig. 6(a), the summation thus has to run over both sites,

$$A_f(\mathbf{q}) \propto \langle f| \sum_{i\in\{1,2\}} e^{i\mathbf{q}\mathbf{R}_i} M_{\mathbf{R}_i} |0\rangle, \tag{4}$$

where $M_{\mathbf{R}_i}$ denotes the dipole matrix element for the RIXS process via site $\mathbf{R}_i$ and $e^{i\mathbf{q}\mathbf{R}_i}$ is the corresponding phase factor. Assuming a dimer with inversion symmetry, the matrix elements on the two sites share the same modulus but may differ in sign, which yields

$$A_f^{\mathrm{inv}}(\mathbf{q}) \propto e^{iq_c d/2} \pm e^{-iq_c d/2}. \tag{5}$$

Since the RIXS intensity is proportional to the amplitude squared, this yields either $\sin^2$ or $\cos^2$ behavior, depending on the parity of $|0\rangle$ and $|f\rangle$. However, a single Ir_2O_9 bioctahedron exhibits mirror symmetry but no inversion symmetry, giving rise to a mixture of $\sin(q_c\, d/2)$ and $\cos(q_c\, d/2)$ terms in the amplitude. In $Ba_3Ti_{3-x}Ir_xO_9$, the bioctahedra in adjacent layers are rotated by π around c with respect to each other, and hence the two different dimer orientations are transformed into each other via inversion; see Fig. 1. Summing the intensities of the two orientations cancels the terms that are odd in q_c such that only $\sin^2(q_c\, d/2)$ and $\cos^2(q_c\, d/2)$ terms survive [42]. For the expected RIXS intensity this yields

$$I_f(q_c) \propto u(q_c) \sin^2(q_c\, d/2) + v(q_c) \cos^2(q_c\, d/2), \tag{6}$$

where the q_c dependences of the prefactors again mainly reflect polarization effects. For $u > v$, this explains the dominant $\sin^2$ behavior described by Eq. (3) and observed in Figs. 6–8 for the peak at 0.35 eV. The opposite behavior with $u < v$ resulting in a dominant $\cos^2$ term is found for the 0.95 eV peak; see Fig. 7. As discussed below, this indicates a spin-flip character of the 0.95 eV peak.

The two dimer sites are displaced along the c axis; thus $\mathbf{q} \cdot \mathbf{d}/2 = q_c\, d/2$. This explains the intensity modulation as a function of l and predicts that dimer features are insensitive to h. This is indeed observed above 0.2 eV; see Figs. 5 and 9. In contrast, the RIXS peak at 0.15 eV exhibits a pronounced

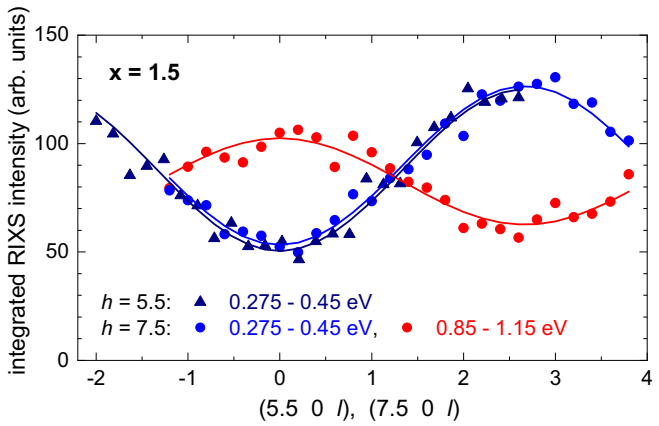

FIG. 7. RIXS interference patterns for $x = 1.5$. The 0.95 eV dimer peak shows $\cos^2(q_c\, d/2)$ behavior (red) [cf. Fig. 4(c)], while a $\sin^2(q_c\, d/2)$ modulation is observed for integration from 0.275 to 0.45 eV, in agreement with Fig. 6(b). Data were collected on a (100) surface with c (nearly) perpendicular to the scattering plane, i.e., rotated by 90° with respect to the geometry used in Fig. 6(b). A finite range of l can be covered by tilting the sample. Solid lines are fits according to $I(l) = a_0 \sin^2(\pi l/2Q_d) + c_0$ and equivalently for the $\cos^2$ curve, using the period $2Q_d = 5.34 \times 2\pi/c$ determined from the data in Fig. 6(b).

h dependence as well as a larger period as a function of l [see Fig. 6(b)], which points to a different microscopic origin; see Sec. V C.

A quasimolecular dimer character has been demonstrated in RIXS measurements on the sister compounds $Ba_3CeIr_2O_9$ and $Ba_3InIr_2O_9$ with two and three holes per dimer, respectively [42,43]. The short intradimer Ir-Ir distance of about 2.5–2.6 Å [35] gives rise to a very large hopping of the

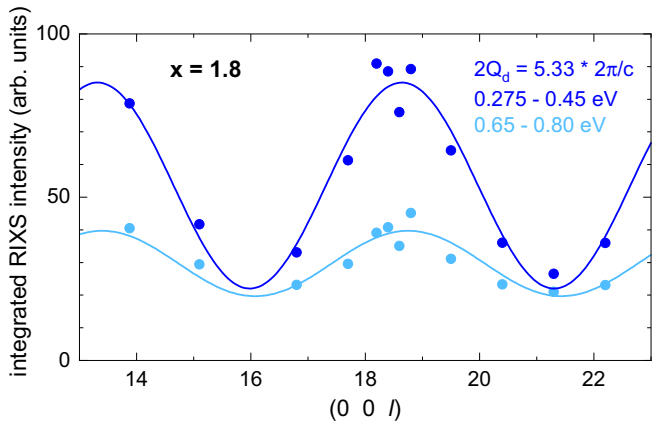

FIG. 8. Modulated RIXS intensity for $x = 1.8$ for large l. In contrast to the $\mathbf{q}$ scans with a fixed energy window depicted in Figs. 6 and 7, the data (symbols) were obtained from a series of RIXS spectra, measured up to 1.5 eV, by integrating the intensity of the dominant peak from 0.275 to 0.45 eV (blue) and from 0.65 to 0.80 eV (light blue). Particularly large values of l are reached by measuring on a (001) surface. Solid lines are fits that yield the period $2Q_d = (5.33 \pm 0.05) \times 2\pi/c$. With the knowledge of the $\sin^2(q_c d/2)$ character from Fig. 6, the large l value allows us to determine the period with high accuracy.

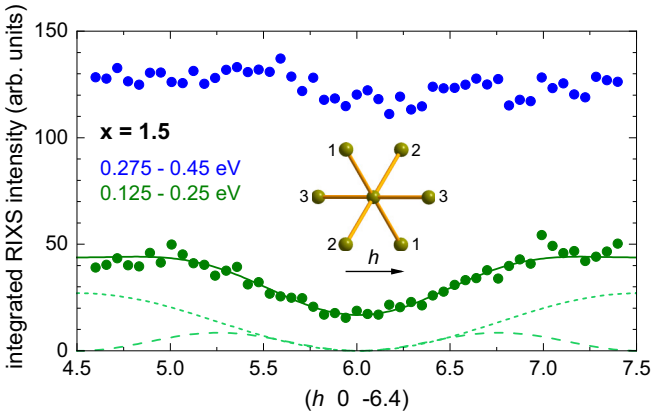

FIG. 9. RIXS interference patterns of $Ba_3Ti_{1.5}Ir_{1.5}O_9$ as a function of h. The dominant dimer peak at 0.35 eV, integrated from 0.275 to 0.45 eV (blue), does not depend on h since the dimer axis is parallel to c; cf. Eq. (3) and Fig. 5. In contrast, the 0.15 eV peak (dark green) shows a modulation with two different periods along h. The solid line depicts the total fit [cf. Eq. (12)], while the light green lines show the two contributions with periods 3 and 3/2 in h. Accordingly, the 0.15 eV peak corresponds to a magnetic excitation for a pair of Ir ions located on neighboring $2a$ and $4f$ sites. Inset: projection of the Ir^{2a}-O-Ir^{4f} bonds onto the ab plane, illustrating the two values of $|\mathbf{q} \cdot \mathbf{r}_i|$ for $\mathbf{q} = (h\ \ 0\ \ 0)$ r.l.u.; cf. Eqs. (7)–(9). The numbers $i \in \{1, 2, 3\}$ denote the six bonds $\pm\mathbf{r}_i$ for a given $2a$ site. The $Ir^{2a}O_6$ octahedra in the neighboring layers are rotated by π around c, giving rise to the identical projection onto the ab plane.

order of 0.5–1 eV [42,43] and a corresponding large splitting of bonding and antibonding quasimolecular orbitals in which the holes are fully delocalized over a given dimer. As in $Ba_3CeIr_2O_9$ with Ce^{4+} ions, the Ir_2O_9 dimers in $Ba_3Ti_{3-x}Ir_xO_9$ host two holes that can be placed in the lowest quasimolecular orbital, giving rise to a nonmagnetic ground state [42]. The RIXS data of $Ba_3CeIr_2O_9$ show three features peaking at about 0.7, 1.0, and 1.2 eV. Similarly, the dimer features in $Ba_3Ti_{3-x}Ir_xO_9$ for large x can be roughly described by three peaks at about 0.35, 0.7, and 0.95 eV, suggesting a reduced energy scale for M = Ti compared with Ce. This tentatively can be ascribed to the larger Ir-Ir distance d, which amounts to 2.65 Å [36] in the Ti compounds and 2.54 Å [42] in $Ba_3CeIr_2O_9$. In a simple picture, a larger Ir-Ir distance d yields reduced hopping and hence a smaller bonding-antibonding splitting. The common character of the dimer states in $Ba_3CeIr_2O_9$ and $Ba_3Ti_{3-x}Ir_xO_9$ is supported by the similar $\mathbf{q}$ dependences. In $Ba_3CeIr_2O_9$, the two lower-energy dimer features show a pronounced $\sin^2(q_c d/2)$ behavior while the third peak at 1.2 eV exhibits $\cos^2(q_c d/2)$ behavior which is strongly suppressed at large l [42]. The same can be observed in $Ba_3Ti_{3-x}Ir_xO_9$. The two features at 0.35 and 0.7 eV show a $\sin^2(q_c d/2)$ intensity modulation (see Figs. 6 and 8), while the third peak at 0.95 eV hardly depends on l for large l [cf. Fig. 4(d)] but indeed shows $\cos^2(q_c d/2)$ behavior for small l; see Figs. 7 and 4(c). For M = Ce, the distinct behavior of the third peak has been shown to arise from the spin-flip character of this excitation [42]. Altogether this suggests that the peak at 0.95 eV for $x = 1.5$ and 1.8 corresponds to a singlet-to-triplet dimer excitation.

In contrast to the related compounds $Ba_3MIr_2O_9$, the physics of $Ba_3Ti_{3-x}Ir_xO_9$ is governed by strong Ti-Ir site disorder. This is highlighted by the coexistence of Ir_2O_9 dimers and single Ir sites in $TiIrO_9$ units for not too small values of x. If dimer formation was energetically unfavorable, it could be avoided for $x = 0.5$, and the same argument holds for single sites at large x. The coexistence thus suggests that neither dimers nor single sites are strongly preferred, pointing towards a random distribution of Ir and Ti ions over the dimer sites, in agreement with previous results [27–29,36]. Combined with the nonmagnetic character of the dimer ground state, this disorder provides the key to understand the surprising x dependence of the magnetic susceptibility; see Fig. 2. For small x, the susceptibility reflects the dominant contribution of dilute $j = 1/2$ moments located on individual Ir sites. With increasing x, however, the relative contribution of nonmagnetic dimers is enhanced, which may even lead to a suppression of $\chi(T)$ upon strongly increasing the Ir content.

C. Magnetic excitation on 2*a* sites

In the following, we address the distinct properties of the 0.15 eV peak [see Figs. 5, 6(b), and 9] and demonstrate how RIXS interferometry allows us to unravel its microscopic origin. For $x = 1.5$, integration of the RIXS intensity as a function of q_c in the energy range 0.125–0.25 eV yields a modulation period $2Q_{2a} = (6.27 \pm 0.08) \times 2\pi/c$ that is about 17% larger than the dimer value $2Q_d$; see Fig. 6(b). The sinusoidal pattern again points towards the interference of scattering on two sites, but their distance projected onto the c axis amounts to $d_{2a} = (2.26 \pm 0.03)$ Å. This agrees with the difference of the z components of $2a$ and $4f$ sites of 2.22 Å measured in x-ray diffraction at 300 K [36], pointing towards the presence of Ir ions on M ($2a$) sites interacting with Ir ions on $4f$ sites. These two sites are also displaced perpendicular to c (cf. Fig. 1), giving rise to the h dependence of the 0.15 eV feature shown in Figs. 5 and 9.

Taking a $2a$ site as the origin of our coordinate frame, it has six $4f$ neighbors at $\pm\mathbf{r}_i$ with $i \in \{1, 2, 3\}$; see right part of Fig. 1 and sketch in the inset of Fig. 9. For simplicity, we consider separate pairs that are built from the Ir ion on the $2a$ site and by *one* Ir neighbor on one of the six neighboring $4f$ sites. This can be motivated by the fact that the 0.15 eV peak is only observed for large x, in which case most of the neighboring bioctahedra will be occupied by two Ir ions with two holes forming a stable singlet in a quasimolecular orbital. We neglect the interaction with such singlets, and we may also neglect those bioctahedra that are occupied by two Ti ions. Relevant to us are the $TiIrO_9$ bioctahedra where the Ir $j = 1/2$ moment on a $4f$ site may interact with one on a $2a$ site, as indicated by the thick black line on the right side of Fig. 1. For such pairs, we expect a sinusoidal intensity modulation $\sin^2(\mathbf{q}\cdot\mathbf{r}_i/2)$, equivalent to Eq. (3). We find

$$\frac{1}{2}\,\mathbf{q}\cdot\mathbf{r}_{1,4} = \pm\Big[(h+2k)\frac{\pi}{3} \pm l\,\frac{\pi}{6.27}\Big], \tag{7}$$

$$\frac{1}{2}\,\mathbf{q}\cdot\mathbf{r}_{2,5} = \pm\Big[(h-k)\frac{\pi}{3} \pm l\,\frac{\pi}{6.27}\Big], \tag{8}$$

$$\frac{1}{2}\,\mathbf{q}\cdot\mathbf{r}_{3,6} = \pm\Big[-(2h+k)\frac{\pi}{3} \pm l\,\frac{\pi}{6.27}\Big] \tag{9}$$

for $2Q_{2a} = 6.27 \times 2\pi/c$. The indices $i \in \{1, 2, 3\}$ and $i \in \{4, 5, 6\}$ of the bonds $\pm\mathbf{r}_i$ refer to $2a$ sites in adjacent layers. The corresponding $Ir^{2a}O_6$ octahedra are rotated by π around c, giving rise to the different signs in front of the l term. The overall sign of $\mathbf{r}_i$ is irrelevant for the $\sin^2(\mathbf{q}\cdot\mathbf{r}_i/2)$ term. Note that all possible pairs yield the same l dependence for $h = k = 0$. This agrees with the sinusoidal modulation with a single period $2Q_{2a}$ observed for the green symbols in Fig. 6(b), which in turn strongly supports the simple picture of separate pairs. The data in Fig. 6(b) were measured with $h = 6.1$, which is nearly equivalent to $h = 0$.

Treating each pair separately, we add the intensities for all six kinds of pairs described by Eqs. (7)–(9). This summation over the two different layers of $Ir^{2a}O_6$ octahedra, rotated by π around c, yields an even function of l, as mentioned above for the dimers,

$$\begin{aligned} I[(h\ k\ l)] &\propto \sum_{i=1\,\text{to}\,6} \sin^2(\mathbf{q}\cdot\mathbf{r}_i/2) \\ &= 3 + \cos\left(l\,\frac{2\pi}{6.27}\right)\cdot\Big[2\sin^2\Big((h+2k)\frac{\pi}{3}\Big) \\ &\quad + 2\sin^2\Big((h-k)\frac{\pi}{3}\Big) \\ &\quad + 2\sin^2\Big((2h+k)\frac{\pi}{3}\Big) - 3\Big]. \end{aligned} \tag{10}$$

The projection of the different $2a$-$4f$ pairs onto the ab plane, sketched in the inset of Fig. 9, yields a characteristic dependence on h and k for constant l that allows us to identify corresponding pair excitations. Figure 9 shows the integrated RIXS intensity of the 0.15 eV peak as a function of h for $k = 0$ and $l = -6.4$. The latter is nearly equivalent to $l \approx 0$ since it is close to a full period $2Q_{2a} = 6.27 \times 2\pi/c$. For this h scan, the model predicts two periods in h, namely, 3 and 3/2,

$$I[(h\ 0\ 0)] \propto 2\sin^2\Big(h\frac{\pi}{3}\Big) + \sin^2\Big(2h\frac{\pi}{3}\Big), \tag{11}$$

due to the two different projections of the $\mathbf{r}_i$ on $(h\ 0\ 0)$. The data in Fig. 9 are well described by a fit (dark green line) based on

$$I_{\text{fit}}(h) = a_0\Big[2\sin^2\Big(h\frac{\pi}{3}\Big) + b_0\sin^2\Big(2h\frac{\pi}{3}\Big)\Big] + c_0, \tag{12}$$

where the two contributions are depicted by the light green lines. The observation of the two periods strongly supports our simple model, even though we find a reduced prefactor $b_0 = 0.63$ for the second term compared with Eq. (11). This scenario of separate pairs of Ir ions on $2a$ and $4f$ sites also explains the intriguing h dependence of the 0.15 eV peak revealed in Fig. 5. For $l = 16.8$, the model indeed predicts a maximum of intensity for $h = 0$ and a minimum for $h = 2$, while the opposite is expected for $l = 19.6$, as observed experimentally.

The excitation energy of 0.15 eV roughly can be motivated via the bonding geometry. The IrO_6 octahedra around the $2a$ and $4f$ sites share a common corner, giving rise to a 180° Ir-O-Ir bond; see Fig. 1. This bonding geometry is equivalent to the case of square-lattice Sr_2IrO_4 with strong Heisenberg exchange J and magnon energies extending up to roughly 0.2 eV [47,48]. For a single bond of two moments coupled by

J, the excitation energy is of the same order of magnitude as found for zone-boundary magnons on the square lattice, which roughly explains the peak energy of 0.15 eV. This scenario of exchange-coupled local moments in contrast to quasimolecular orbitals is based on the fact that hopping t is significantly smaller in corner-sharing geometry than for face-sharing octahedra. The ratio of the on-site Coulomb repulsion U over t is then large enough to suppress a quasimolecular character and the physics is described by two $j = 1/2$ moments coupled by an exchange interaction $J \propto t^2/U$. Note that a similar RIXS feature was observed at 0.23 eV in $Ba_3InIr_2O_9$ with three holes per dimer and magnetic $j_{\rm dim} = 3/2$ dimer moments [43]. There, about 7% of Ir ions were observed on the In 2a sites.

Altogether, our results provide strong evidence for the identification of the 0.15 eV peak as a magnetic excitation of a pair of exchange-coupled Ir $j = 1/2$ moments located on neighboring 2a and 4f sites. This assignment is further supported by the observed symmetry, i.e., the dominant $\sin^2(\mathbf{q}\cdot\mathbf{r}_i/2)$ character of the interference pattern plotted in Figs. 6(b) and 9; cf. Eq. (12). The corner-sharing octahedra of a 2a-4f pair show the same orientation; see Fig. 1. In this case we expect the minus sign in Eq. (5) for a spin-flip excitation, in agreement with the observed $\sin^2(\mathbf{q}\cdot\mathbf{r}_i/2)$ behavior. In contrast, the two IrO_6 octahedra of a face-sharing dimer are rotated by π around c with respect to each other. For the intradimer spin flip at 0.95 eV, this contributes a further minus sign and yields the $\cos^2(q_c\, d/2)$ behavior observed in Fig. 7.

VI. CONCLUSIONS

The physics of $Ba_3Ti_{3-x}Ir_xO_9$ is dominated by strong disorder. The similar radii and equal valence of Ir^{4+} and Ti^{4+} ions yield mixed crystals with pronounced Ir-Ti site mixing. For $x \geqslant 0.5$, our RIXS spectra of samples with $x \in \{0.3, 0.5, 1.5, 1.8\}$ demonstrate the coexistence of single-site $j = 1/2$ moments and Ir_2O_9 dimers, as expected for a random distribution of Ir and Ti ions. Individual spin-orbit-entangled $j = 1/2$ moments prevail for small Ir content x while the density of Ir_2O_9 dimers increases with x. Due to the large intradimer hopping, the dimers host quasimolecular orbitals in which the holes are fully delocalized over the two dimer sites. Both holes occupy the lowest binding orbital in the dimer ground state, forming a nonmagnetic $j_{\rm dim} = 0$ singlet. The coexistence of nonmagnetic dimers and $j = 1/2$ moments explains the at first sight unconventional behavior of the magnetic susceptibility which is very similar for $x = 0.5$ and 1.5, i.e., for two samples in which the concentration of magnetic Ir ions differs by a factor of 3.

These compounds offer a remarkable example for the unusual role that disorder may play in a cluster Mott insulator. Substituting a magnetic ion by a nonmagnetic one typically yields a vacancy in the magnetic system. In a cluster, however, it changes the character of the magnetic moment. In $Ba_3Ti_{3-x}Ir_xO_9$, cation disorder gives rise to different kinds of magnetic moments, and the different moments experience very different coupling strengths. On a dimer, the energy scale for singlet-to-triplet excitations is given by the RIXS peak at 0.95 eV, reflecting the large intradimer hopping. In contrast, the large spatial separation between dimers strongly suppresses interdimer interactions [73]. Considering, e.g., $j = 1/2$ moments on neighboring $IrTiO_9$ bioctahedra, we expect exchange interactions on the order of meV, i.e., three orders of magnitude smaller than the intradimer singlet-to-triplet excitation energy within Ir_2O_9 units. Additionally, we observe pairs of exchange-coupled $j = 1/2$ moments that arise from Ir ions located on adjacent 2a and 4f sites. These are connected via a 180° bond that yields a large Heisenberg exchange coupling J similar to the case of square-lattice Sr_2IrO_4, giving rise to a magnetic excitation at 0.15 eV.

RIXS interferometry enabled us to unravel this complex disorder scenario. The RIXS spectra and, in particular, the $\mathbf{q}$ dependence of the RIXS intensity provide clear fingerprints of the different types of moments. The excitations of local single-site $j = 1/2$ moments are independent of $\mathbf{q}$. In contrast, a sinusoidal modulation of the RIXS intensity of orbital excitations is a characteristic hallmark of quasimolecular dimer orbitals, and a predominant $\sin^2(\mathbf{q}\cdot\mathbf{r}/2)$ or $\cos^2(\mathbf{q}\cdot\mathbf{r}/2)$ behavior typifies the symmetry and character of the excited states. The RIXS studies of the sister compounds $Ba_3CeIr_2O_9$ and $Ba_3InIr_2O_9$ [42,43] were focused on establishing the distinct quasimolecular character for two or three holes per dimer. In $Ba_3Ti_{3-x}Ir_xO_9$, the periodicity of the modulation allows us to identify which *sites* contribute to a given excitation. We can distinguish Ir_2O_9 dimers from 2a-4f pairs via the distinct modulation period along l as well as via the absence or presence of a characteristic modulation along h or k. We expect that our results will trigger many further experimental investigations to exploit the stunning power of RIXS interferometry to study the electronic structure of dimers, trimers, and larger clusters, even in the presence of disorder.

ACKNOWLEDGMENTS

We thank A. Revelli for experimental support and useful discussions. We gratefully acknowledge the European Synchrotron Radiation Facility for providing beam time and technical support. Furthermore, we acknowledge funding from the Deutsche Forschungsgemeinschaft (DFG, German Research Foundation) through Project No. 277146847 – CRC 1238 (Projects No. A02 and No. B03) and Project No. 247310070 – CRC 1143 (Project No. A05). M.H. acknowledges partial funding by the Knut and Alice Wallenberg Foundation as part of the Wallenberg Academy Fellows project and by the Swedish Research Council through Grant No. 2017.0157.

APPENDIX A: SELF-ABSORPTION CORRECTION

The use of hard x-rays allows us to study the RIXS intensity over a large range of $\mathbf{q}$. This nevertheless requires substantial changes in the experimental geometry, which in turn affect self-absorption effects. The central parameters are $\theta_{\rm in}$ and $\theta_{\rm out}$, which correspond to the angles between the sample surface and the incident and emitted beams, respectively. For instance, for small $\theta_{\rm in}$ and a scattering angle 2θ close to 90°, the incident x-ray photons are absorbed near the surface, which reduces the absorption probability for the reemitted photons, giving rise to a large signal. In contrast, the detected intensity is suppressed for $\theta_{\rm in}$ close to 90° in combination with a small value of $\theta_{\rm out}$. This geometrical aspect of

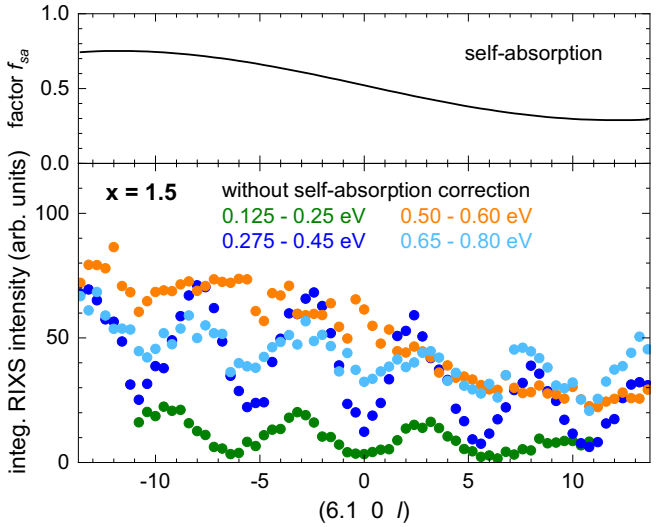

FIG. 10. Effect of self-absorption on the RIXS data. Bottom panel: RIXS intensity of $Ba_3Ti_{1.5}Ir_{1.5}O_9$ at $T = 20$ K as a function of l. The data were integrated over the indicated energy windows. For comparison, Fig. 6(b) shows the same data after self-absorption correction, i.e., divided by the factor f_{sa} shown in the top panel; cf. Eq. (A1).

self-absorption is captured by the factor [51]

$$f_{sa} = \frac{1}{1 + \frac{\sin\theta_{\text{in}}}{\sin\theta_{\text{out}}}}. \tag{A1}$$

All of our data are corrected for this self-absorption factor f_{sa}. To demonstrate the effect, the bottom panel of Fig. 10 shows the corresponding data of Fig. 6(b) prior to self-absorption correction, while the top panel plots the factor f_{sa} for the employed geometry. We emphasize that the assignment of RIXS features in this paper is mainly based on the modulation period of the RIXS intensity. This is not affected by the slowly varying factor f_{sa}. Furthermore, the data of the spin-orbit exciton peak at 0.57 eV nicely corroborate our approach. The

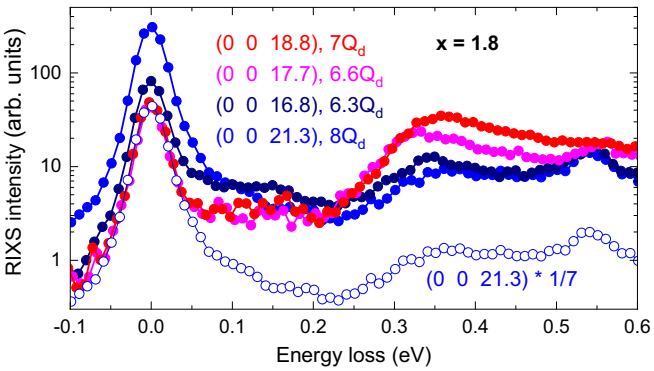

FIG. 11. RIXS spectra of $Ba_3Ti_{1.2}Ir_{1.8}O_9$ at $T = 20$ K. The data of Fig. 4(d) are plotted on a logarithmic intensity scale to include the entire elastic line. Additionally, open symbols depict the data for (0 0 21.3) multiplied by 1/7.

measured intensity, integrated from 0.50 to 0.60 eV, closely follows the shape of f_{sa}; see Fig. 10. After correction, the RIXS intensity of this feature is constant within the experimental uncertainty, as expected for a predominantly local, single-site excitation.

APPENDIX B: ELASTIC LINE

For incident π polarization, the elastic line can be suppressed for a scattering angle $2\theta \approx 90°$. This is illustrated by plotting the data of Fig. 4(d) on a logarithmic scale; see Fig. 11. The data were measured with $2\theta \approx 82°$, 87°, 94°, and 112° for $l = 16.8$, 17.7, 18.8, and 21.3, respectively. For $2\theta \approx 87°$ and 94°, the elastic line is weak. The open symbols in Fig. 11 depict the data with the strongest elastic line for $2\theta \approx 112°$ scaled down by a factor 1/7. The result for negative energy loss shows that a change of 2θ affects the intensity of the elastic line but not its line shape. Furthermore, this plot highlights the presence of a weak inelastic contribution between about 0.05 and 0.2 eV in all four data sets. The corresponding RIXS peak at 0.15 eV is addressed in Sec. V C.

[1] J. Knolle and R. Moessner, A field guide to spin liquids, Annu. Rev. Condens. Matter Phys. **10**, 451 (2019).
[2] Y. Shimizu, K. Miyagawa, K. Kanoda, M. Maesato, and G. Saito, Spin Liquid State in an Organic Mott Insulator with a Triangular Lattice, Phys. Rev. Lett. **91**, 107001 (2003).
[3] M. Yamashita, N. Nakata, Y. Senshu, M. Nagata, H. M. Yamamoto, R. Kato, T. Shibauchi, and Y. Matsuda, Highly mobile gapless excitations in a two-dimensional candidate quantum spin liquid, Science **328**, 1246 (2010).
[4] T.-H. Han, J. S. Helton, S. Chu, D. G. Nocera, J. A. Rodriguez-Rivera, C. Broholm, and Y. S. Lee, Fractionalized excitations in the spin-liquid state of a kagome-lattice antiferromagnet, Nature (London) **492**, 406 (2012).
[5] G. Jackeli and G. Khaliullin, Mott Insulators in the Strong Spin-Orbit Coupling Limit: From Heisenberg to a Quantum Compass and Kitaev Models, Phys. Rev. Lett. **102**, 017205 (2009).
[6] W. Witczak-Krempa, G. Chen, Y. B. Kim, and L. Balents, Correlated quantum phenomena in the strong spin-orbit regime, Annu. Rev. Condens. Matter Phys. **5**, 57 (2014).
[7] J. G. Rau, E. K.-H. Lee, and H.-Y. Kee, Spin-orbit physics giving rise to novel phases in correlated systems: Iridates and related materials, Annu. Rev. Condens. Matter Phys. **7**, 195 (2016).
[8] R. Schaffer, E. K.-H. Lee, B.-J. Yang, and Y. B. Kim, Recent progress on correlated electron systems with strong spin-orbit coupling, Rep. Prog. Phys. **79**, 094504 (2016).
[9] S. M. Winter, A. A. Tsirlin, M. Daghofer, J. van den Brink, Y. Singh, P. Gegenwart, and R. Valentí, Models and materials for generalized Kitaev magnetism, J. Phys.: Condens. Matter **29**, 493002 (2017).
[10] M. Hermanns, I. Kimchi, and J. Knolle, Physics of the Kitaev model: Fractionalization, dynamic correlations, and material connections, Annu. Rev. Condens. Matter Phys. **9**, 17 (2018).

[11] G. Cao and P. Schlottmann, The challenge of spin-orbit-tuned ground states in iridates, Rep. Prog. Phys. **81**, 042502 (2018).

[12] H. Takagi, T. Takayama, G. Jackeli, G. Khaliullin and S. E. Nagler, Concept and realization of Kitaev quantum spin liquids, Nat. Rev. Phys. **1**, 264 (2019).

[13] Y. Motome and J. Nasu, Hunting Majorana fermions in Kitaev magnets, J. Phys. Soc. Jpn. **89**, 012002 (2020).

[14] T. Takayama, J. Chaloupka, A. Smerald, G. Khaliullin, and H. Takagi, Spin-orbit-entangled electronic phases in 4*d* and 5*d* transition-metal compounds, J. Phys. Soc. Jpn. **90**, 062001 (2021).

[15] S. Trebst and C. Hickey, Kitaev materials, Phys. Rep. **950**, 1 (2022).

[16] S. H. Chun, J.-W. Kim, J. Kim, H. Zheng, C. C. Stoumpos, C. D. Malliakas, J. F. Mitchell, K. Mehlawat, Y. Singh, Y. Choi, T. Gog, A. Al-Zein, M. Moretti Sala, M. Krisch, J. Chaloupka, G. Jackeli, G. Khaliullin, and B. J. Kim, Direct evidence for dominant bond-directional interactions in a honeycomb lattice iridate Na_2IrO_3, Nat. Phys. **11**, 462 (2015).

[17] M. Magnaterra, K. Hopfer, Ch. J. Sahle, M. Moretti Sala, G. Monaco, J. Attig, C. Hickey, I.-M. Pietsch, F. Breitner, P. Gegenwart, M. H. Upton, J. Kim, S. Trebst, P. H. M. van Loosdrecht, J. van den Brink, and M. Grüninger, RIXS observation of bond-directional nearest-neighbor excitations in the Kitaev material Na_2IrO_3, arXiv:2301.08340.

[18] Y. Singh and P. Gegenwart, Antiferromagnetic Mott insulating state in single crystals of the honeycomb lattice material Na_2IrO_3, Phys. Rev. B **82**, 064412 (2010).

[19] Y. Singh, S. Manni, J. Reuther, T. Berlijn, R. Thomale, W. Ku, S. Trebst, and P. Gegenwart, Relevance of the Heisenberg-Kitaev Model for the Honeycomb Lattice Iridates A_2IrO_3, Phys. Rev. Lett. **108**, 127203 (2012).

[20] V. M. Katukuri, S. Nishimoto, V. Yushankhai, A. Stoyanova, H. Kandpal, S. Choi, R. Coldea, I. Rousochatzakis, L. Hozoi, and J. van den Brink, Kitaev interactions between $j = 1/2$ moments in honeycomb Na_2IrO_3 are large and ferromagnetic: insights from *ab initio* quantum chemistry calculations, New J. Phys. **16**, 013056 (2014).

[21] J. G. Rau, E. K.-H. Lee, and H.-Y. Kee, Generic Spin Model for the Honeycomb Iridates beyond the Kitaev Limit, Phys. Rev. Lett. **112**, 077204 (2014).

[22] S. M. Winter, Y. Li, H. O. Jeschke, and R. Valentí, Challenges in design of Kitaev materials: Magnetic interactions from competing energy scales, Phys. Rev. B **93**, 214431 (2016).

[23] K. Kitagawa, T. Takayama, Y. Matsumoto, A. Kato, R. Takano, Y. Kishimoto, S. Bette, R. Dinnebier, G. Jackeli, and H. Takagi, A spin-orbital-entangled quantum liquid on a honeycomb lattice, Nature (London) **554**, 341 (2018).

[24] R. Yadav, R. Ray, M. S. Eldeeb, S. Nishimoto, L. Hozoi, and J. van den Brink, Strong Effect of Hydrogen Order on Magnetic Kitaev Interactions in $H_3LiIr_2O_6$, Phys. Rev. Lett. **121**, 197203 (2018).

[25] Y. Li, S. M. Winter, and R. Valentí, Role of Hydrogen in the Spin-Orbital-Entangled Quantum Liquid Candidate $H_3LiIr_2O_6$, Phys. Rev. Lett. **121**, 247202 (2018).

[26] S. Wang, L. Zhang, and F. Wang, Possible quantum paraelectric state in Kitaev spin liquid candidate $H_3LiIr_2O_6$, Sci. China Phys. Mech. Astron. **63**, 117411 (2020).

[27] T. Dey, A. V. Mahajan, P. Khuntia, M. Baenitz, B. Koteswararao, and F. C. Chou, Spin-liquid behavior in $J_{\rm eff} = 1/2$ triangular lattice compound $Ba_3IrTi_2O_9$, Phys. Rev. B **86**, 140405(R) (2012).

[28] R. Kumar, D. Sheptyakov, P. Khuntia, K. Rolfs, P. G. Freeman, H. M. Rønnow, T. Dey, M. Baenitz, and A. V. Mahajan, $Ba_3M_xTi_{3-x}O_9$ (M = Ir, Rh): A family of $5d/4d$-based diluted quantum spin liquids, Phys. Rev. B **94**, 174410 (2016).

[29] W.-J. Lee, S.-H. Do, Sungwon Yoon, S. Lee, Y. S. Choi, D. J. Jang, M. Brando, M. Lee, E. S. Choi, S. Ji, Z. H. Jang, B. J. Suh, and K.-Y. Choi, Putative spin liquid in the triangle-based iridate $Ba_3IrTi_2O_9$, Phys. Rev. B **96**, 014432 (2017).

[30] T. Dey, M. Majumder, J. C. Orain, A. Senyshyn, M. Prinz-Zwick, S. Bachus, Y. Tokiwa, F. Bert, P. Khuntia, N. Büttgen, A. A. Tsirlin, and P. Gegenwart, Persistent low-temperature spin dynamics in the mixed-valence iridate $Ba_3InIr_2O_9$, Phys. Rev. B **96**, 174411 (2017).

[31] A. Nag, S. Middey, S. Bhowal, S. K. Panda, R. Mathieu, J. C. Orain, F. Bert, P. Mendels, P. G. Freeman, M. Mansson, H. M. Ronnow, M. Telling, P. K. Biswas, D. Sheptyakov, S. D. Kaushik, V. Siruguri, C. Meneghini, D. D. Sarma, I. Dasgupta, and S. Ray, Origin of the Spin-Orbital Liquid State in a Nearly $J = 0$ Iridate $Ba_3ZnIr_2O_9$, Phys. Rev. Lett. **116**, 097205 (2016).

[32] A. Nag, S. Bhowal, M. Moretti Sala, A. Efimenko, I. Dasgupta, and S. Ray, Hopping-Induced Ground-State Magnetism in 6*H* Perovskite Iridates, Phys. Rev. Lett. **123**, 017201 (2019).

[33] M. S. Khan, A. Bandyopadhyay, A. Nag, V. Kumar, A. V. Mahajan, and S. Ray, Magnetic ground state of the distorted 6*H* perovskite $Ba_3CdIr_2O_9$, Phys. Rev. B **100**, 064423 (2019).

[34] S. Kumar, S. K. Panda, M. M. Patidar, S. K. Ojha, P. Mandal, G. Das, J. W. Freeland, V. Ganesan, P. J. Baker, and S. Middey, Spin-liquid behavior of the three-dimensional magnetic system $Ba_3NiIr_2O_9$ with $S = 1$, Phys. Rev. B **103**, 184405 (2021).

[35] Y. Doi and Y. Hinatsu, The structural and magnetic characterization of 6H-perovskite-type oxides $Ba_3LnIr_2O_9$ (Ln = Y, lanthanides), J. Phys.: Condens. Matter **16**, 2849 (2004).

[36] T. Sakamoto, Y. Doi, and Y. Hinatsu, Crystal structures and magnetic properties of 6H-perovskite-type oxides $Ba_3MIr_2O_9$ (M = Mg, Ca, Sc, Ti, Zn, Sr, Zr, Cd and In), J. Solid State Chem. **179**, 2595 (2006).

[37] L. T. Nguyen and R. J. Cava, Hexagonal perovskites as quantum materials, Chem. Rev. **121**, 2935 (2021).

[38] S. J. Kim, M. D. Smith, J. Darriet, and H.-C. zur Loye, Crystal growth of new perovskite and perovskite related iridates: $Ba_3LiIr_2O_9$, $Ba_3NaIr_2O_9$, and $Ba_{3.44}K_{1.56}Ir_2O_{10}$, J. Solid State Chem. **177**, 1493 (2004).

[39] T. Dey, R. Kumar, A. V. Mahajan, S. D. Kaushik, and V. Siruguri, Unconventional magnetism in the spin-orbit-driven Mott insulators $Ba_3MIr_2O_9$ (M=Sc, Y), Phys. Rev. B **89**, 205101 (2014).

[40] C. Garg, D. Roy, M. Lonsky, P. Manuel, A. Cervellino, J. Müller, M. Kabir, and S. Nair, Evolution of the structural, magnetic, and electronic properties of the triple perovskite $Ba_3CoIr_2O_9$, Phys. Rev. B **103**, 014437 (2021).

[41] S. V. Streltsov and D. I. Khomskii, Covalent bonds against magnetism in transition metal compounds, Proc. Natl. Acad. Sci. USA **113**, 10491 (2016).

[42] A. Revelli, M. Moretti Sala, G. Monaco, P. Becker, L. Bohatý, M. Hermanns, T. C. Koethe, T. Fröhlich, P. Warzanowski, T. Lorenz, S. V. Streltsov, P. H. M. van Loosdrecht, D. I. Khomskii, J. van den Brink, and M. Grüninger, Resonant in-

elastic x-ray incarnation of Young's double-slit experiment, Sci. Adv. **5**, eaav4020 (2019).

[43] A. Revelli, M. Moretti Sala, G. Monaco, M. Magnaterra, J. Attig, L. Peterlini, T. Dey, A. A. Tsirlin, P. Gegenwart, T. Fröhlich, M. Braden, C. Grams, J. Hemberger, P. Becker, P. H. M. van Loosdrecht, D. I. Khomskii, J. van den Brink, M. Hermanns, and M. Grüninger, Quasimolecular electronic structure of the spin-liquid candidate $Ba_3InIr_2O_9$, Phys. Rev. B **106**, 155107 (2022).

[44] D. I. Khomskii and S. V. Streltsov, Orbital effects in solids: Basics, recent progress, and opportunities, Chem. Rev. **121**, 2992 (2021).

[45] M. Becker, M. Hermanns, B. Bauer, M. Garst, and S. Trebst, Spin-orbit physics of $j = 1/2$ Mott insulators on the triangular lattice, Phys. Rev. B **91**, 155135 (2015).

[46] A. Catuneanu, J. G. Rau, H.-S. Kim, and H.-Y. Kee, Magnetic orders proximal to the Kitaev limit in frustrated triangular systems: Application to $Ba_3IrTi_2O_9$, Phys. Rev. B **92**, 165108 (2015).

[47] J. Kim, D. Casa, M. H. Upton, T. Gog, Y.-J. Kim, J. F. Mitchell, M. van Veenendaal, M. Daghofer, J. van den Brink, G. Khaliullin, and B. J. Kim, Magnetic Excitation Spectra of Sr_2IrO_4 Probed by Resonant Inelastic X-Ray Scattering: Establishing Links to Cuprate Superconductors, Phys. Rev. Lett. **108**, 177003 (2012).

[48] J. Kim, M. Daghofer, A. H. Said, T. Gog, J. van den Brink, G. Khaliullin, and B. J. Kim, Excitonic quasiparticles in a spin-orbit Mott insulator, Nat. Commun. **5**, 4453 (2014).

[49] M. Moretti Sala, C. Henriquet, L. Simonelli, R. Verbeni, and G. Monaco, High energy-resolution set-up for Ir L_3 edge RIXS experiments, J. Electron Spectrosc. Relat. Phenom. **188**, 150 (2013).

[50] M. Moretti Sala, K. Martel, C. Henriquet, A. Al Zein, L. Simonelli, Ch. J. Sahle, H. Gonzalez, M.-C. Lagier, C. Ponchut, S. Huotari, R. Verbeni, M. Krisch, and G. Monaco, A high-energy-resolution resonant inelastic x-ray scattering spectrometer at ID20 of the European Synchrotron Radiation Facility, J. Synchrotron Radiat. **25**, 580 (2018).

[51] M. Minola, G. Dellea, H. Gretarsson, Y. Y. Peng, Y. Lu, J. Porras, T. Loew, F. Yakhou, N. B. Brookes, Y. B. Huang, J. Pelliciari, T. Schmitt, G. Ghiringhelli, B. Keimer, L. Braicovich, and M. Le Tacon, Collective Nature of Spin Excitations in Superconducting Cuprates Probed by Resonant Inelastic X-Ray Scattering, Phys. Rev. Lett. **114**, 217003 (2015).

[52] M. Moretti Sala, S. Boseggia, D. F. McMorrow, and G. Monaco, Resonant X-Ray Scattering and the $j_{\text{eff}} = 1/2$ Electronic Ground State in Iridate Perovskites, Phys. Rev. Lett. **112**, 026403 (2014).

[53] H. Gretarsson, J. P. Clancy, X. Liu, J. P. Hill, E. Bozin, Y. Singh, S. Manni, P. Gegenwart, J. Kim, A. H. Said, D. Casa, T. Gog, M. H. Upton, H.-S. Kim, J. Yu, V. M. Katukuri, L. Hozoi, J. van den Brink, and Y.-J. Kim, Crystal-Field Splitting and Correlation Effect on the Electronic Structure of A_2IrO_3, Phys. Rev. Lett. **110**, 076402 (2013).

[54] X. Liu, V. M. Katukuri, L. Hozoi, Wei-Guo Yin, M. P. M. Dean, M. H. Upton, Jungho Kim, D. Casa, A. Said, T. Gog, T. F. Qi, G. Cao, A. M. Tsvelik, J. van den Brink, and J. P. Hill, Testing the Validity of the Strong Spin-Orbit-Coupling Limit for Octahedrally Coordinated Iridate Compounds in a Model System Sr_3CuIrO_6, Phys. Rev. Lett. **109**, 157401 (2012).

[55] A. Revelli, C. C. Loo, D. Kiese, P. Becker, T. Fröhlich, T. Lorenz, M. Moretti Sala, G. Monaco, F. L. Buessen, J. Attig, M. Hermanns, S. V. Streltsov, D. I. Khomskii, J. van den Brink, M. Braden, P. H. M. van Loosdrecht, S. Trebst, A. Paramekanti, and M. Grüninger, Spin-orbit entangled $j = 1/2$ moments in Ba_2CeIrO_6: A frustrated fcc quantum magnet, Phys. Rev. B **100**, 085139 (2019).

[56] A. Ruiz, N. P. Breznay, M. Li, I. Rousochatzakis, A. Allen, I. Zinda, V. Nagarajan, G. Lopez, Z. Islam, M. H. Upton, J. Kim, A. H. Said, X.-R. Huang, T. Gog, D. Casa, R. J. Birgeneau, J. D. Koralek, J. G. Analytis, N. B. Perkins, and A. Frano, Magnon-spinon dichotomy in the Kitaev hyperhoneycomb β-Li_2IrO_3, Phys. Rev. B **103**, 184404 (2021).

[57] A. de la Torre, B. Zager, F. Bahrami, M. DiScala, J. R. Chamorro, M. H. Upton, G. Fabbris, D. Haskel, D. Casa, T. M. McQueen, F. Tafti, and K. W. Plumb, Enhanced hybridization in the electronic ground state of the intercalated honeycomb iridate $Ag_3LiIr_2O_6$, Phys. Rev. B **104**, L100416 (2021).

[58] M. Rossi, M. Retegan, C. Giacobbe, R. Fumagalli, A. Efimenko, T. Kulka, K. Wohlfeld, A. I. Gubanov, and M. Moretti Sala, Possibility to realize spin-orbit-induced correlated physics in iridium fluorides, Phys. Rev. B **95**, 235161 (2017).

[59] D. Reig-i-Plessis, T. A. Johnson, K. Lu, Q. Chen, J. P. C. Ruff, M. H. Upton, T. J. Williams, S. Calder, H. D. Zhou, J. P. Clancy, A. A. Aczel, and G. J. MacDougall, Structural, electronic, and magnetic properties of nearly ideal $J_{\text{eff}} = 1/2$ iridium halides, Phys. Rev. Mater. **4**, 124407 (2020).

[60] N. Khan, D. Prishchenko, M. H. Upton, V. G. Mazurenko, and A. A. Tsirlin, Towards cubic symmetry for Ir^{4+}: Structure and magnetism of the antifluorite K_2IrBr_6, Phys. Rev. B **103**, 125158 (2021).

[61] D. I. Khomskii, K. I. Kugel, A. O. Sboychakov, and S. V. Streltsov, Role of local geometry in the spin and orbital structure of transition metal compounds, J. Exp. Theor. Phys. **122**, 484 (2016).

[62] J. G. Vale, C. D. Dashwood, E. Paris, L. S. I. Veiga, M. GarciaFernandez, A. Nag, A. Walters, K.-J. Zhou, I.-M. Pietsch, A. Jesche, P. Gegenwart, R. Coldea, T. Schmitt, and D. F. McMorrow, High-resolution resonant inelastic x-ray scattering study of the electron-phonon coupling in honeycomb α-Li_2IrO_3, Phys. Rev. B **100**, 224303 (2019).

[63] B. Yuan, J. P. Clancy, A. M. Cook, C. M. Thompson, J. Greedan, G. Cao, B. C. Jeon, T. W. Noh, M. H. Upton, D. Casa, T. Gog, A. Paramekanti and Y.-J. Kim, Determination of Hund's coupling in 5*d* oxides using resonant inelastic x-ray scattering, Phys. Rev. B **95**, 235114 (2017).

[64] M. Kusch, V. M. Katukuri, N. A. Bogdanov, B. Büchner, T. Dey, D. V. Efremov, J. E. Hamann-Borrero, B. H. Kim, M. Krisch, A. Maljuk, M. Moretti Sala, S. Wurmehl, G. Aslan-Cansever, M. Sturza, L. Hozoi, J. van den Brink, and J. Geck, Observation of heavy spin-orbit excitons propagating in a nonmagnetic background: The case of $(Ba, Sr)_2YIrO_6$, Phys. Rev. B **97**, 064421 (2018).

[65] A. Nag, S. Bhowal, A. Chakraborty, M. M. Sala, A. Efimenko, F. Bert, P. K. Biswas, A. D. Hillier, M. Itoh, S. D. Kaushik, V. Siruguri, C. Meneghini, I. Dasgupta, and S. Ray, Origin of magnetic moments and presence of spin-orbit singlets in Ba_2YIrO_6, Phys. Rev. B **98**, 014431 (2018).

[66] Y. Wang, R. Wang, J. Kim, M. H. Upton, D. Casa, T. Gog, G. Cao, G. Kotliar, M. P. M. Dean, and X. Liu, Direct Detection of Dimer Orbitals in $Ba_5AlIr_2O_{11}$, Phys. Rev. Lett. **122**, 106401 (2019).

[67] V. M. Katukuri, X. Lu, D. E. McNally, M. Dantz, V. N. Strocov, M. Moretti Sala, M. H. Upton, J. Terzic, G. Cao, O. V. Yazyev, and T. Schmitt, Charge ordering in Ir dimers in the ground state of $Ba_5AlIr_2O_{11}$, Phys. Rev. B **105**, 075114 (2022).

[68] A. Revelli, M. Moretti Sala, G. Monaco, C. Hickey, P. Becker, F. Freund, A. Jesche, P. Gegenwart, T. Eschmann, F. L. Buessen, S. Trebst, P. H. M. van Loosdrecht, J. van den Brink, and M. Grüninger, Fingerprints of Kitaev physics in the magnetic excitations of honeycomb iridates, Phys. Rev. Res. **2**, 043094 (2020).

[69] F. Gel'mukhanov and H. Agren, Resonant inelastic x-ray scattering with symmetry-selective excitation, Phys. Rev. A **49**, 4378 (1994).

[70] Y. Ma, X-ray absorption, emission, and resonant inelastic scattering in solids, Phys. Rev. B **49**, 5799 (1994).

[71] Y. Ma and M. Blume, Interference of fluorescence x rays and coherent excitation of core levels, Rev. Sci. Instrum. **66**, 1543 (1995).

[72] F. Gel'mukhanov, M. Odelius, S. P. Polyutov, A. Föhlisch, and V. Kimberg, Dynamics of resonant x-ray and Auger scattering, Rev. Mod. Phys. **93**, 035001 (2021).

[73] S. Bhowal, S. Ganguly, and I. Dasgupta, Spinorbit coupling driven novel magnetism in d^5 6H-perovskite iridates $Ba_3IrTi_2O_9$ and $Ba_3TiIr_2O_9$, J. Phys.: Condens. Matter **31**, 185802 (2019).